Click Here for Full Article

Permeability-porosity relationships in seafloor vent deposits: Dependence on pore evolution processes

Wenlu Zhu,[1] Margaret K. Tivey,[2] Hilary Gittings,[3] and Paul R. Craddock[2]

[1]   Systematic laboratory measurements of permeability and porosity were conducted on three large vent structures from the Mothra Hydrothermal vent field on the Endeavor segment of the Juan de Fuca Ridge. Geometric means of permeability values obtained from a probe permeameter are 5.9×10^{-15} m^2 for Phang, a tall sulfide-dominated spire that was not actively venting when sampled; 1.4×10^{-14} m^2 for Roane, a lower-temperature spire with dense macrofaunal communities growing on its sides that was venting diffuse fluid of <300°C; and 1.6×10^{-14} m^2 for Finn, an active black smoker with a well-defined inner conduit that was venting 302°C fluids prior to recovery. Twenty-three cylindrical cores were then taken from these vent structures. Permeability and porosity of the drill cores were determined on the basis of Darcy's law and Boyle's law, respectively. Permeability values range from $\sim 10^{-15}$ to 10^{-13} m^2 for core samples from Phang, from $\sim 10^{-15}$ to 10^{-12} m^2 for cores from Roane, and from $\sim 10^{-15}$ to 3×10^{-13} m^2 for cores from Finn, in good agreement with the probe permeability measurements. Permeability and porosity relationships are best described by two different power law relationships with exponents of ~ 9 (group I) and ~ 3 (group II). Microstructural analyses reveal that the difference in the two permeability-porosity relationships reflects different mineral precipitation processes as pore space evolves within different parts of the vent structures, either with angular sulfide grains depositing as aggregates that block fluid paths very efficiently (group I), or by late stage amorphous silica that coats existing grains and reduces fluid paths more gradually (group II). The results suggest that quantification of permeability and porosity relationships leads to a better understanding of pore evolution processes. Correctly identifying permeability and porosity relationships is an important first step toward accurately estimating fluid distribution, flow rate, and environmental conditions within seafloor vent deposits, which has important consequences for chimney growth and biological communities that reside within and on vent structures.

Citation: Zhu, W., M. K. Tivey, H. Gittings, and P. R. Craddock (2007), Permeability-porosity relationships in seafloor vent deposits: Dependence on pore evolution processes, *J. Geophys. Res.*, *112*, B05208, doi:10.1029/2006JB004716.

1. Introduction

[2]   At seafloor hydrothermal vent sites, vent deposits form from complex interactions among hot (ca. 350°C) metal-, sulfide-, and silica-rich hydrothermal fluid, cold (ca. 2°C) sulfate-rich seawater, solid substrates, ± biological organisms [e.g., *Haymon*, 1983; *Goldfarb et al.*, 1983]. These deposits are modern-day equivalents of some types of volcanic-associated massive sulfide deposits preserved in ophiolite and island arc terranes of orogenic belts [e.g., *Oudin*, 1983; *Oudin and Constantinou*, 1984; *Haymon et al.*, 1984; *Koski*, 1987]. Significant insight into the factors that control formation and evolution of the deposits has been gained through analyses of vent fluid and solid samples, and by coupling these analyses with geochemical modeling techniques [e.g., *Janecky and Seyfried*, 1984; *Bowers et al.*, 1985; *Janecky and Shanks*, 1988; *Tivey and McDuff*, 1990; *Edmond et al.*, 1995; *Tivey*, 1995; *Tivey et al.*, 1995, 1999]. More recently, novel in situ sensors have been used to examine the temporal and spatial heterogeneity of environmental conditions both within and at exteriors of deposits, in an effort to better understand controls on mineral deposition, the distributions of micro-, macro-, and megafauna, and the ways in which these organisms gain energy and nutrients from mixtures of ambient seawater and hot vent fluids [e.g., *Cary et al.*, 1998; *Luther et al.*, 2001; *Le Bris et al.*, 2005].

[3]   While conducting these in situ measurements is costly and technically challenging, to interpret the data collected

[1]Department of Geology and Geophysics, WHOI, Woods Hole, Massachusetts, USA.
[2]Department of Marine Chemistry and Geochemistry, WHOI, Woods Hole, Massachusetts, USA.
[3]Department of Geology and Geophysics, University of Wisconsin-Madison, Madison, Wisconsin, USA.

often requires accurate modeling of fluid flow, mixing, and fluid distributions within the structures. Interactions between cold seawater and the hot, metal- and sulfide-rich vent fluids exert primary control on environmental conditions such as pore fluid temperature, pH and chemical composition, within and at the exteriors of vent deposits. Conversely, these environmental conditions affect flow through pore space via processes that modify pore space and connectivity. In essence, processes such as mineral precipitation, dissolution and thermal cracking modify fluid flow, altering environmental conditions. Clearly, understanding these feedbacks, and making accurate estimates of the magnitudes and directions of fluid flow within the structures and how they change with time, hinges upon a better understanding of permeability, and of permeability-porosity relationships. Because fluids flow through void space, permeability, a physical property that quantifies the ability of fluid to flow through a material, and porosity, the volume fraction of void in a material, are closely related.

[4] To address a lack of data on permeability and the relationship between permeability and porosity in vent deposits, we conducted laboratory measurements on three large hydrothermal vent samples recovered from the Mothra Hydrothermal field on the Endeavour segment of the Juan de Fuca Ridge (JFR). It is important to realize that the permeability and porosity measurements we made only provide a "snapshot" of the constantly evolving vent structure. Our study, however, illuminates how the permeability-porosity relationships depend upon mineral grain distribution and pore geometry within different portions of the deposits, which evolve with time as fluid temperatures and chemistries change. Results of our spatial "snapshots" within different portions of the vent structures can thus be viewed as an analog to temporal "snapshots" at a single location, and thus interpreted as a permeability-porosity relationship that reflects the evolution of pore space and permeability.

[5] As summarized recently by Bernabé et al. [2003], "there is no 'universal' porosity-permeability relationship valid in all porous media." There are good correlations found between permeability and porosity, however, for some types of samples, particularly when pore evolution processes (i.e., the processes that change pore space) are considered. Types of pore evolution processes include compaction during burial, depressurization during uplift, deformation under tectonic stresses, and diagenesis and metamorphic reactions, including precipitation and dissolution. These processes create and/or destroy both effective and noneffective porosity, with the former affecting permeability, and with both affecting specific evolution permeability-porosity relationships (EPPR). At seafloor hydrothermal vents, hot fluids are transported through the vent structures, cool, deposit different minerals and alter the pore space, thus the dependence of permeability-porosity relationships on mineral compositions observed in this study reflects the evolution processes of the deposits. By identifying the permeability-porosity relationship associated with mineral composition and pore geometry, our data not only provide laboratory constraints on the permeability and porosity of seafloor sulfide deposits, but more importantly also provide new insights into the evolution of hydrothermal

vent structures and environmental conditions within and at the exteriors of these deposits.

2. Fluid Flow in Active Seafloor Vent Deposits

[6] Fluid flow within heterogeneous seafloor vent deposits is dependent on the relative permeabilities of different parts of the structures (e.g., of the open conduits versus high-porosity/permeability zones versus lower-porosity/permeability walls), the velocity of fluid flow within the conduits/high-permeability regions, and the density contrast between the hot vent fluid within the deposit and the cold seawater exterior to the structure [e.g., Tivey and McDuff, 1990; Woods and Delaney, 1992]. Variations in rates of vent fluid flow out of the structures, and of seawater into the structures, affect local fluid chemistry and temperature [e.g., Tivey and McDuff, 1990; Tivey, 1995, 2004]. Styles of fluid flow and mixing are extremely important in determining (1) the saturation state of minerals at various points within the structure (and consequently whether minerals will precipitate or dissolve [e.g., Janecky and Seyfried, 1984; Bowers et al., 1985; Janecky and Shanks, 1988; Tivey and McDuff, 1990; Tivey, 1995; Tivey et al., 1995, 1999], (2) whether conditions are suitable for microorganisms within the structure [e.g., McCollom and Shock, 1997; Shock and Holland, 2004; Tivey, 2004], and (3) whether conditions are suitable for macro- and mega-fauna on vent structure surfaces [e.g., Juniper et al., 1992; Cary et al., 1998; Luther et al., 2001; Sarrazin et al., 2002; Le Bris et al., 2005].

[7] While vent fields may remain active for tens of years or more, individual vents are ephemeral, with passages clogged on timescales of months to years, and flow redirected on similar or shorter timescales as pore space within the structure changes, dominantly from mineral precipitation, but also from mineral dissolution and thermal cracking. There are many different styles of venting, with fluids exiting rapidly through black smoker chimneys with open central conduits, venting more slowly from sides of diffusing spires (e.g., white smoker chimneys) that lack a central open conduit, percolating through overlying ledges (flanges) that trap pools of hot fluid, and/or percolating from the sides of porous/permeable sections of deposits [e.g., Haymon and Kastner, 1981; Goldfarb et al., 1983; Haymon, 1983; Koski et al., 1984, 1994; Hannington and Scott, 1988; Paradis et al., 1988; Delaney et al., 1992; Robigou et al., 1993; Fouquet et al., 1993; Tivey et al., 1995]. For each of these sample types, mineral precipitation (± mineral dissolution and/or thermal cracking) changes pore geometry, which in turn modifies directions and magnitudes of fluid flow. Our goals in this study included determining permeabilities of different portions of vent deposits, and examining the relationships that exist between permeability and porosity to determine whether there are EPPRs specific to sample types, and/or to stages of vent deposit formation. Correctly identifying EPPRs can aid in predicting how flow rate will change over time in different parts of vent structures, which directly affects mineral saturation and the composition of the deposits. For example, a key question for many hydrothermal structures is whether there are cascading feedbacks that lead to clogging, or, alternatively, whether the feedback is such that fluid flow is
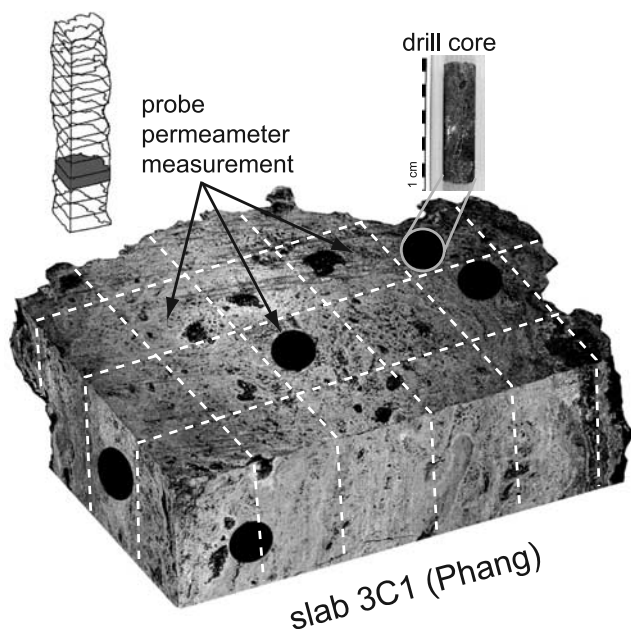
Figure 1. Diagram showing sampling of the Phang structure and slab 3C1 from Phang. The grids show where probe permeability measurements took place. The black circles indicate where drill cores were taken after the probe measurements.

maintained in certain portions of the structures. These better estimates of how quickly different parts of structures seal themselves, or alternatively of the relative constancy of flow, can provide better estimates of environmental conditions (including flow rate, pH, temperature, chemical composition), which has important consequences for micro-, macro-, and mega-fauna residing within and on exteriors of vent structures.

3. Methods

[8] The successful recovery of four large vent structures from the Mothra Hydrothermal vent field on the Endeavor segment of the JFR [*Delaney et al.*, 2001; *Kelley et al.*, 2001] provided a rare opportunity to conduct systematic laboratory measurements of physical properties of vent deposits. The samples used in this study are from Phang, a tall sulfide dominated spire that was not actively venting when sampled; Roane, a lower-temperature spire with dense macrofaunal communities growing on its sides, that was venting diffuse, not focused, fluid of <300°C; and Finn, an active black smoker with a well-defined inner conduit, that was venting 302°C fluids prior to recovery [*Delaney et al.*, 2001; *Kristall et al.*, 2006].

[9] As described by *Kristall et al.* [2006], the recovered samples were cut vertically in half, and then one half was cut again vertically into two quarters; one of the quarters was then sectioned into multiple horizontal slabs, each ~10 cm thick (Figure 1). Recognizing that vent deposits are very heterogeneous, which renders the permeability value highly scale sensitive, we began our study by conducting permeability measurements on these large slabs

($\sim20 \times 30 \times 10$ cm^3) using a portable probe permeameter prior to taking core samples. The probe permeameter uses a steady state flow technique based on Darcy's law. Gas (in this case, air) is injected into the rock sample through a small compressible tip, flows into the sample and then back to the surface. The injection pressure is monitored with an absolute pressure transducer. The flow rate is measured by three electronic mass flow meters. One caveat of using this technique is that the inferred permeability is only appropriate for homogeneous and isotropic materials [*Sutherland et al.*, 1993]. Because vent deposits are generally quite heterogeneous, estimates of permeability for the whole slab can be highly inaccurate. To circumvent this problem, we divided the slabs into areas small enough ($\sim4 \times$ the probe tip diameter) to be considered approximately homogeneous (Figure 1). Permeability measurements were done at the center of each grid, and the inferred permeabilities represent the local values at each grid.

[10] While a probe permeameter provides quick estimation of permeability, the obtained probe permeability values are not unidirectional, because the flow pattern around the probe tip is unknown [*Sutherland et al.*, 1993]. Moreover, there are no porosity measurements available for the slabs. To obtain permeability-porosity relationships of the vent deposits, a total of twenty-three cylindrical cores with diameters of 2.54 cm and various lengths were taken from the slabs after probe measurements were made (Figure 1). A helium porosimeter (UltraPore™300) and a nitrogen permeameter (Ultraperm™400) from Core Laboratories Instruments were used to obtain porosity and permeability of each core. The porosimeter uses Boyle's law to determine pore volume from the expansion of a known mass of helium into a calibrated sample holder, whereas the permeameter uses Darcy's law to determine permeability by measuring the steady state flow rate through the sample under a given pressure gradient.

[11] During the permeability measurements, a moderate confining pressure was needed to prevent leakage between the sample surface and the cup holder. Application of a confining pressure usually causes closure of pore space, and thin cracks are generally more compliant than equal dimensional pores [e.g., *Walsh*, 1965]. Permeability is closely related to pore geometry. Thus changes in pressure subsequently affect permeability. To check the pressure dependence of permeability in the vent deposit samples, we applied hydrostatic pressures of 0.5 to 2.75 MPa to the vent samples, and we conducted permeability measurements at different isotropic pressures. Cyclic loadings were performed on the samples to check the reproducibility of the measurements: Once the maximum pressure of 2.75 MPa (i.e., 400 psi) was reached, we unloaded the sample to ambient pressure, and then conducted a second loading cycle and measured permeability at various pressures.

[12] Following collection of permeability and porosity data, petrographic thin sections were made from each core, and the distribution of pore space (void size, void continuity, etc.) was examined using reflected and transmitted light petrography. Volume percent of sulfide was determined from these thin sections using image analysis of 20 images per thin section. Image analysis was not used to distinguish clay versus amorphous silica versus pore space, as each appears gray in reflected light. Instead volume percent silica
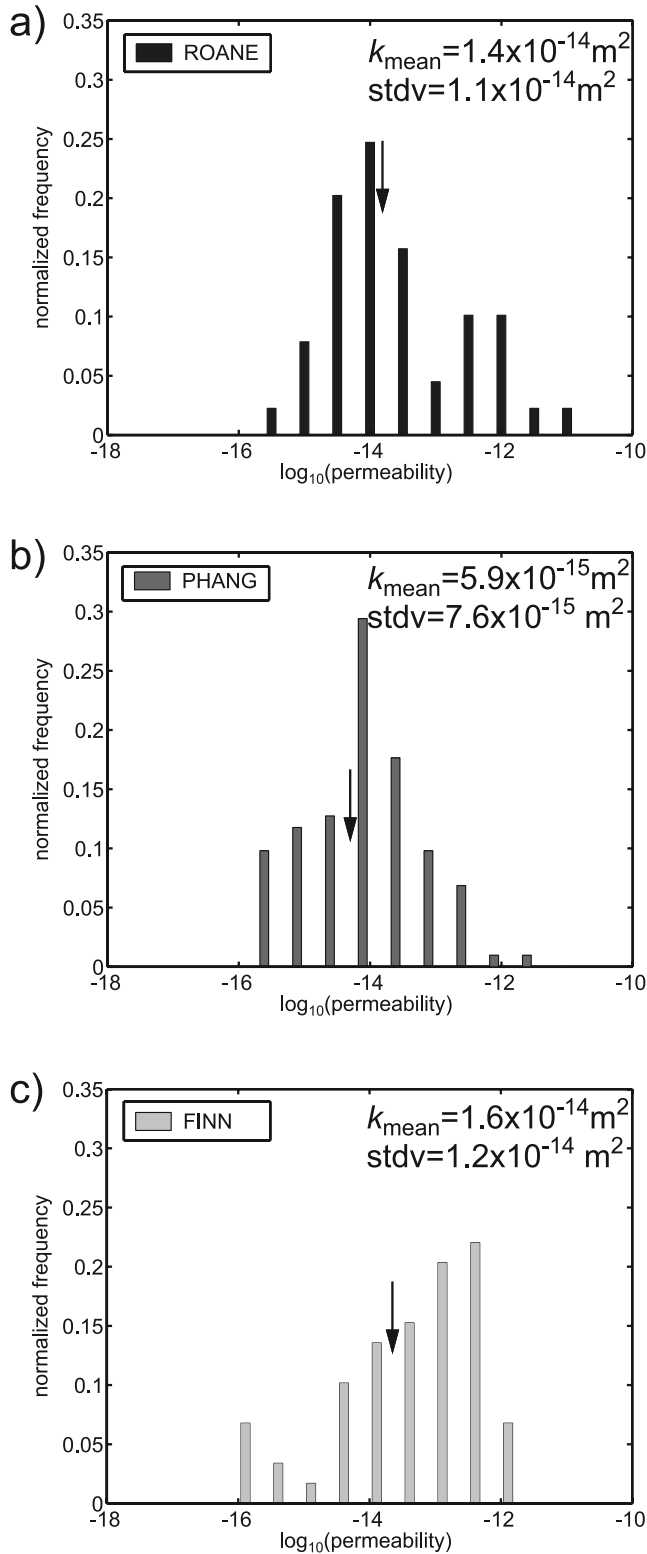
Figure 2. Histograms of permeability values for (a) Roane, (b) Phang, and (c) Finn, obtained using a probe permeameter. The geometrical means of the permeability values are indicated by arrows. Standard deviations are also given.

with or without trace amounts of clay was determined by difference, given the core porosity and assuming that the volume percent sulfide for each thin section was representative of the core. Estimates of the temperatures at which different mineral phases would become saturated as hydrothermal fluid cools conductively, and of the volume of each mineral phase that would precipitate from a kilogram of vent fluid assuming equilibrium conditions at different temperatures, were made using the computer program EQ3/6 [*Wolery*, 1992a, 1992b; *Wolery and Daveler*, 1992]. The SUPCRT92 thermodynamic database [*Johnson et al.*, 1992] was used, with data added for $MgSO_4$ and $NaSO_4$ species [*McCollom and Shock*, 1997], HCl (aq) [*Sverjensky et al.*, 1991], and $FeCl_2$(aq) and CuCl (aq) at temperatures above 300°C [*Ding and Seyfried*, 1992a, 1992b]. Grotto and Hulk fluid compositions (from the main Endeavour field, where vent fluids and structures are ammonia-rich and silica-rich, respectively, relative to at most vent fields [*Butterfield et al.*, 1994; *Lilley et al.*, 1993]) were used for these calculations because of a lack of published data for Roane vent fluid.

4. Results

[13] Measurements of permeability using the probe permeameter on four blocks from Finn, two slabs from Roane, and three slabs from Phang yielded ~300 permeability values (Figure 2). The geometric means derived from probe permeability data are 1.6×10^{-14} m^2 for Finn, 1.4×10^{-14} m^2 for Roane, and 5.9×10^{-15} m^2 for Phang, respectively. These data include measurements conducted in 3 orthogonal orientations of the slab; no significant permeability anisotropy was detected. As shown in Figure 2, the mean of the permeability values (expressed in logarithmic form) of the inactive low-temperature spire Phang is a half order of magnitude lower than those of the active smokers Finn and Roane. While the standard deviation of the permeability values of Phang is the lowest (7.6×10^{-15} m^2 for Phang, 1.1×10^{-14} m^2 for Roane, and 1.2×10^{-14} m^2 for Finn), the lower mean value renders the coefficient of variation (i.e., standard deviation/mean) of Phang as the highest (1.29 for Phang, 0.78 for Roane, and 0.75 for Finn). This result, however, also reflects that the standard deviation and the coefficient of variation are very sensitive to outliers in non-Gaussian data sets such as those shown here (e.g., Figure 2b). An alternative measure that is not similarly biased by outliers in a non-Gaussian data set is the interquartile range, which is defined as the difference between the 75th percentile (3rd quartile) and 25th percentile (1st quartile), and which results in a more stable measure of statistical variation. The interquartile ranges of data for Phang, Roane and Finn are 1.8×10^{-15} m^2, 6.3×10^{-15} m^2, and 1.1×10^{-14} m^2 respectively. On the basis of these data, and that our permeability values do not display a Gaussian distribution, we conclude that among the low-temperature spires, the permeability structure of Phang is less heterogeneous than the permeability structure of either Finn or Roane.

[14] As shown in Table 1, permeability and porosity values of core samples obtained from different confining pressures show qualitatively similar trends. In general, the permeability values obtained during the first and second loading cycles are comparable (Figure 3), which provides
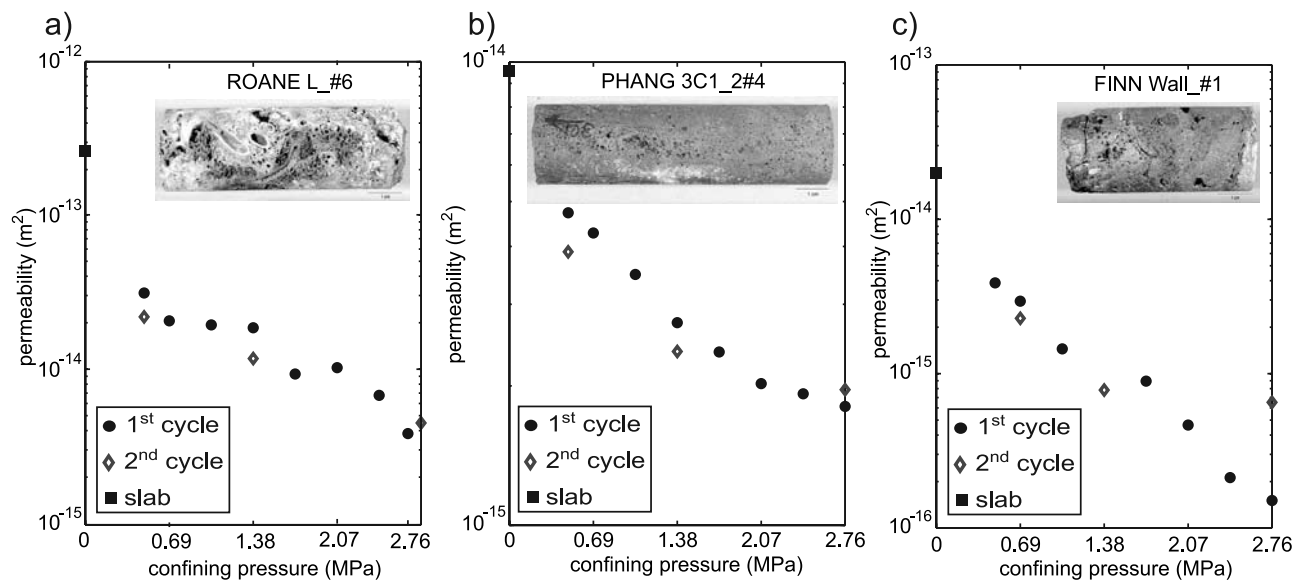
Figure 3. Pressure dependence of permeability in core samples from (a) Roane, (b) Phang, and (c) Finn hydrothermal vent structures. The solid circles are permeability values obtained during the initial loading cycle, and the empty diamonds are values obtained during the second loading cycle after releasing the initial load. The solid squares are permeability values obtained using the probe permeameter at the spots where the cores subsequently were drilled.

reassuring evidence that the applied pressure does not cause irreversible damage to the samples. While increasing confining pressure decreases permeability and porosity, the permeability-porosity relationships at 200, 300 and 400 psi (the highest confinement used in this study) are very similar, which again demonstrates that the applied confinement did

not significantly alter the permeability-porosity relationships.

[15] Permeability and porosity data at a confining pressure of 300 psi (~2.07 MPa) are shown in Figure 4 to demonstrate our findings. Data from Roane cores (Figure 4a) exhibit two different power law relationships, one with an

Table 1. Permeability and Porosity Values of Drill Cores From Mothra Hydrothermal Samples[a]

Sample ID	Probe k, $\times 10^{-15}$ m^2 14.5 psi (0.1 MPa)	ϕ, %	k, $\times 10^{-15}$ m^2	ϕ, %	k, $\times 10^{-15}$ m^2	ϕ, %	k, $\times 10^{-15}$ m^2
		200 psi (1.38 MPa)		300 psi (2.07 MPa)		400 psi (2.76 MPa)	
		Phang					
1A2#1	17.5	17.8	4.6	17.4	3.5	17.2	2.9
1A2#7	8.6	18.5	50.9	18.5	49.9	18.3	49.9
1A2#14	7.1	12.6	1.4	12.7	1.2	12.6	1.14
1A2_2#8	2.0	17.4	8.4	17.1	7.5	16.8	6.7
1A2_3#8	34.5	20.6	82.3	20.0	80.9	19.7	79.2
3C1_1#2	67.4	15.6	5.1	15.4	3.7	14.9	2.1
3C1_1#4	2.1	10.7	1.0	13.0	0.5	12.4	0.1
3C1_1#7	149.9	15.0	0.9	14.4	0.8	14.3	0.6
3C1_2#4	9.6	13.9	5.4	13.9	3.2	13.1	2.5
3C1_2#9	18.6	16.2	6.6	15.6	5.3	15.1	4.0
		Roane					
RnB_#10	5.1	15.3	6.2	15.1	5.1	14.6	4.8
RnB_#12	9247.9	19.7	183.0	19.4	176.8	19.4	171.3
RnB_2#1	197.1	19.7	6.4	19.7	3.9	18.8	3.2
RnB_2#11	2.1	14.9	2.4	14.7	1.8	14.3	1.3
RnB_2#16	2.2	17.7	7.4	18.1	5.0	16.9	3.7
RnL_#6	77.4	26.0	21.7	25.4	18.5	24.8	13.8
RnL_#13	974.9	31.4	2382.5	26.6	2294.6	26.2	2131.5
RnL_#16	0.3	15.3	2.0	14.9	1.5	14.7	1.2
RnL_#21	64.1	28.1	147.8	27.6	144.3	27.4	138.6
		Finn					
FnB#18	112.4	28.4	374.0	28.0	359.7	27.7	351.5
FnB#20	123.4	24.8	506.2	24.4	465.9	24.3	450.2
FnWL#1	19.9	15.0	2.0	14.3	1.1	13.9	0.7
FnWL#2	1.1	14.8	1.2	14.6	0.8	14.1	0.1

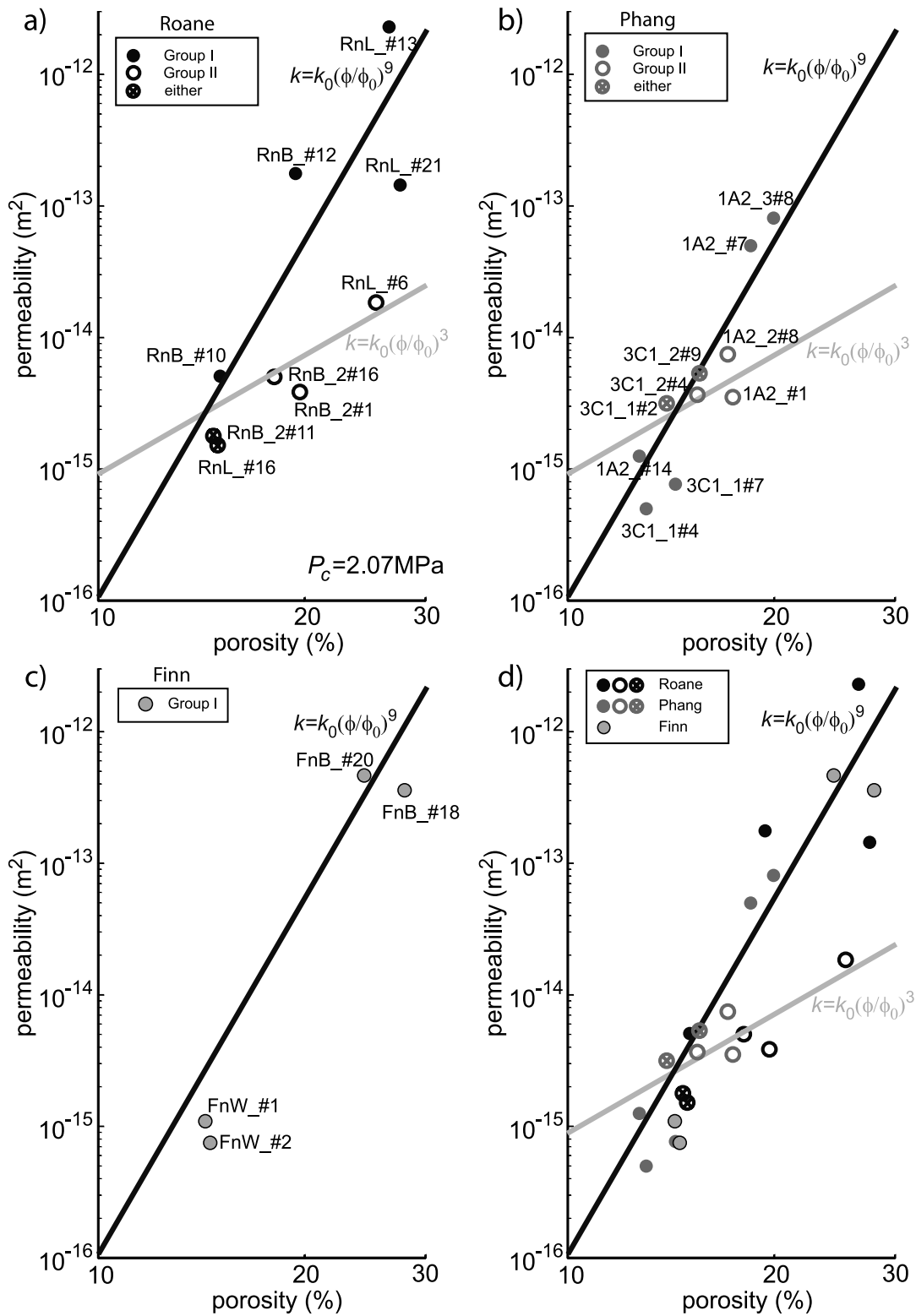[a]Permeability values from a probe permeameter at the sites where drill cores were obtained are also included.

Figure 4. Two distinctive permeability-porosity trends are found in data from (a) Roane cores and (b) Phang cores, while data from (c) Finn cores fit a single permeability-porosity trend. (d) Permeability-porosity data for all the measured cores from Roane, Phang, and Finn.
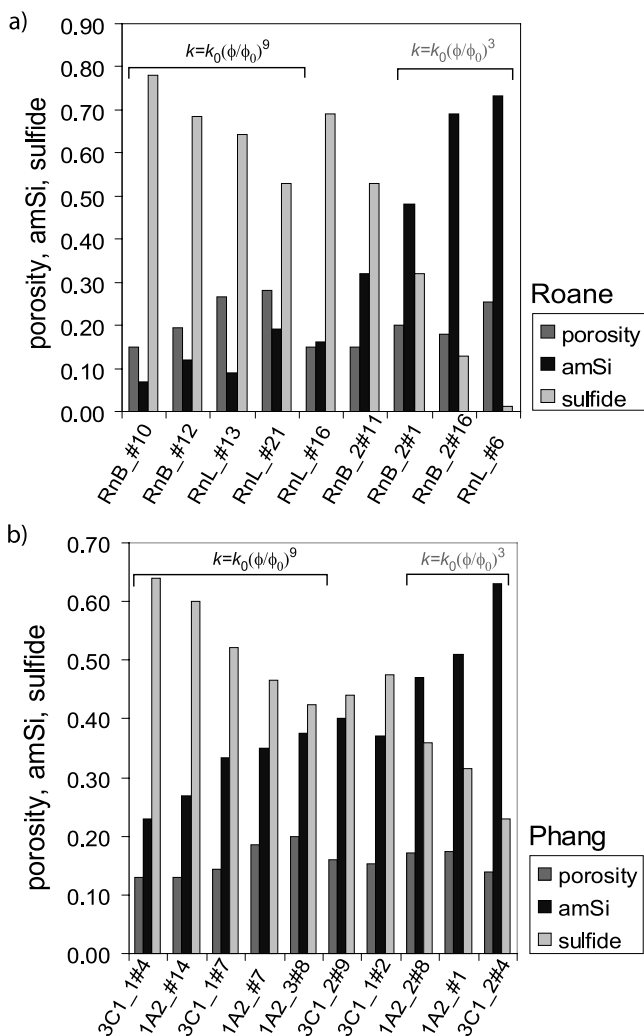
Figure 5. Histograms of proportions of porosity, sulfide, and amorphous silica in (a) Roane cores and (b) Phang cores. Porosity was measured for each core, sulfide percent determined using image analysis of 20 images per thin section for each core, and amorphous silica determined by difference.

exponent of ~9 (group I), and another with an exponent of ~3 (group II). The Roane group I cores exhibit minor amorphous silica with and without trace amounts of clay (<20 vol%), abundant sulfide (≥53 vol%; grains range in size from 50 to >250 μm and are anhedral to euhedral), with porosity inversely correlated with sulfide abundance (Figure 5 and Figures 6a–6c). The distribution of amorphous silica and clay in these cores is patchy, and coatings of amorphous silica, where present, are thin (~10 μm). These group I cores were all taken from the inner portion of Roane, within 14 cm of its axis. In contrast, Roane group II cores all contain abundant amorphous silica with and without trace amounts of clay (>48 vol%), with amorphous silica present as a thick (≥50 μm) layer coating sulfide and clay; the cores are sulfide-poor relative to the group I cores (≤32 vol%), with amorphous silica abundances inversely correlated with sulfide abundances (Figure 5). Compared to group I cores (Figures 6a–6c), amorphous silica precipitation prevails in group II cores (Figures 6d–6f). These cores were all taken from the outer portion of Roane, >14 cm

from its vertical axis. Data from cores RnB_2#11 and RnL_#16 fit either trend; they were cored from the outer portion of the sample but are sulfide-rich (53 and 69 vol%) relative to group II cores. Core RnL_#16 is silica-poor (16 vol%) with the coating of silica varying from 0 to 50 μm, while core RnB_2#11 exhibits more abundant silica (32 vol%) as a thick coating (50 to 150 μm).

[16] Permeability-porosity relationships for data from Phang cores show similar trends as those observed for Roane core data (Figure 4b). The five cores with data that lie along a trend with an exponent of ~9 (Phang group I), cores 1A2_3#8, 1A2_#7, 3C1_1#7, 3C1_1#4, and 1A2_#14, each exhibit a patchy distribution of amorphous silica with or without trace amounts of clay, with areas where amorphous silica is absent; these areas also exhibit larger sulfide grain size (dominantly wurtzite, 100 to >250 μm; Figures 7a–7c). For each of these cores, vol% amorphous silica (23 to 38 vol%) is less than, and inversely correlated with, vol% sulfide (64 to 43 vol%; grains range in size from 30 to >250 μm and are anhedral to euhedral) and with porosity (Figure 5). In contrast, for Phang group II cores 1A2_2_#8, 3C1_2#4, and 1A2_#1, amorphous silica is more abundant than sulfide (47 to 63 vol% versus 36 to 23 vol%) and present throughout (except in a few isolated wurtzite-rich patches), occurring as a thin to thick coating (up to 30 to 150 μm; Figures 7d–7f). Data from these cores plot along a trend with exponent ~3. As in the Phang group I cores and Roane group II cores, amorphous silica abundances are inversely correlated with sulfide abundances. Data from cores 3C1_2#9 and 3C1_1#2 could fit either trend; vol% sulfide exceeds vol% silica, but silica is present throughout these cores as a thin (<40 μm, average 10 μm) coating in 3C1_2#9, and as a thicker (10–150 μm) coating in 3C1_1#2.

[17] Compared to Roane and Phang, it was more difficult to obtain cylindrical cores from Finn (the large black smoker chimney) because the chalcopyrite layer (inner conduit) broke apart during coring, in part because of the presence of cracks filled with anhydrite (likely formed because of thermal cracking), and to the weakness of the coupling between the inner chalcopyrite layer and sulfide/anhydrite outer portion. The results from four cores, two that include part of the chalcopyrite inner layer, and two from the outer part of the wall, follow the steeper permeability-porosity trend ($k \propto \phi^9$, group I, Figures 4c and 4d). These cores contain only minor to trace amorphous silica, and are composed dominantly of sulfide with minor anhydrite.

[18] Information about the temperature at which sulfide minerals and amorphous silica become saturated as vent fluid transits through a structure such as Roane and cools conductively was gained through use of thermodynamic modeling calculations. With cooling of either Grotto or Hulk vent fluids, which are similar to Mothra vent fluids in terms of ammonia concentration and pH at 25°C [Kristall et al., 2006], but are venting at ~350°C, only sulfide minerals are predicted to precipitate as fluids cool from ~350°C to ~200°C (Figure 8). Chalcopyrite is the dominant phase predicted to precipitate at temperatures greater than 280°C and pyrite at lower temperatures. Sphalerite is predicted to precipitate as Hulk and Grotto fluids cool below ~275°C and 200°C, respectively. Amorphous silica is predicted to precipitate at ~200°C, and by the time the fluids cool to 155 to 170°C, roughly ten times more silica
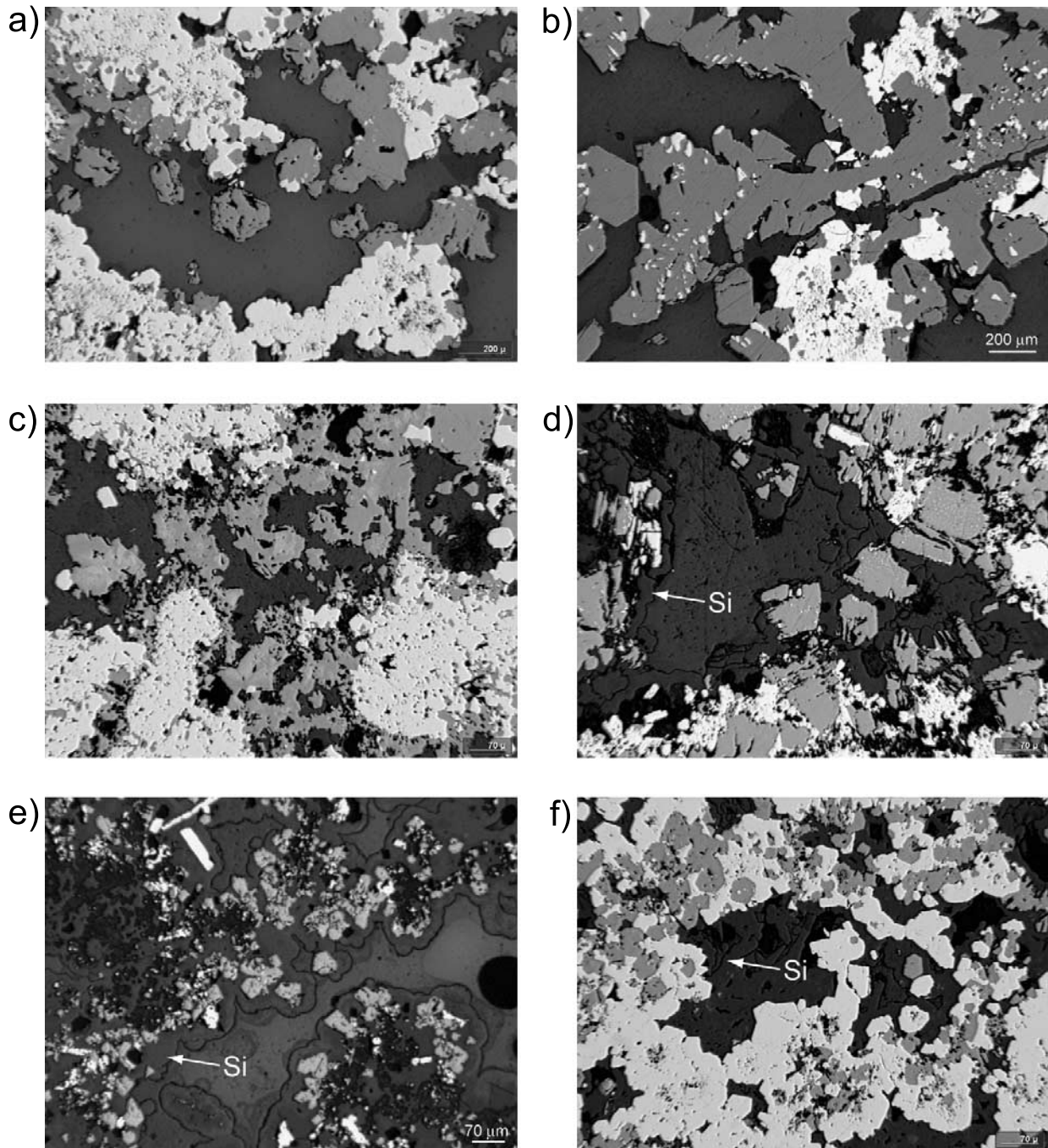
Figure 6. Photomicrographs (reflected light) from interior portions of Roane where little to no amorphous silica is present, from cores (a) RnL_#13, (b) RnL_#21, (c) RnB_#10, and exteriors of Roane where amorphous silica is present as a late stage coating, from cores (d) RnB_2#1, (e) RnB_2#16, and (f) RnB_2#11. Minerals shown are wurtzite (light gray), pyrite or chalcopyrite (white) and amorphous silica (Si) (dark gray). Void space (epoxy filled) also appears dark gray in reflected light.

by volume is predicted to precipitate relative to pyrite, sphalerite, and chalcopyrite.

5. Discussion

5.1. Processes Resulting in Porosity and Permeability Decrease

[19] Two trends are observed in the permeability-porosity data for the drill cores from the three Mothra spires, one with a steeper trend ($k \propto \phi^9$) and one with a shallower trend ($k \propto \phi^3$). In interpreting the data, we recognize that uncertainties in permeability measurements are usually large compared to other physical properties such as porosity. In addition, the low number of cores with porosity greater than 20% in this study likely reflects difficulties in obtaining cores from less consolidated parts of the vent structures. Taking these uncertainties into account, the two permeability and porosity trends defined by the measurements alone
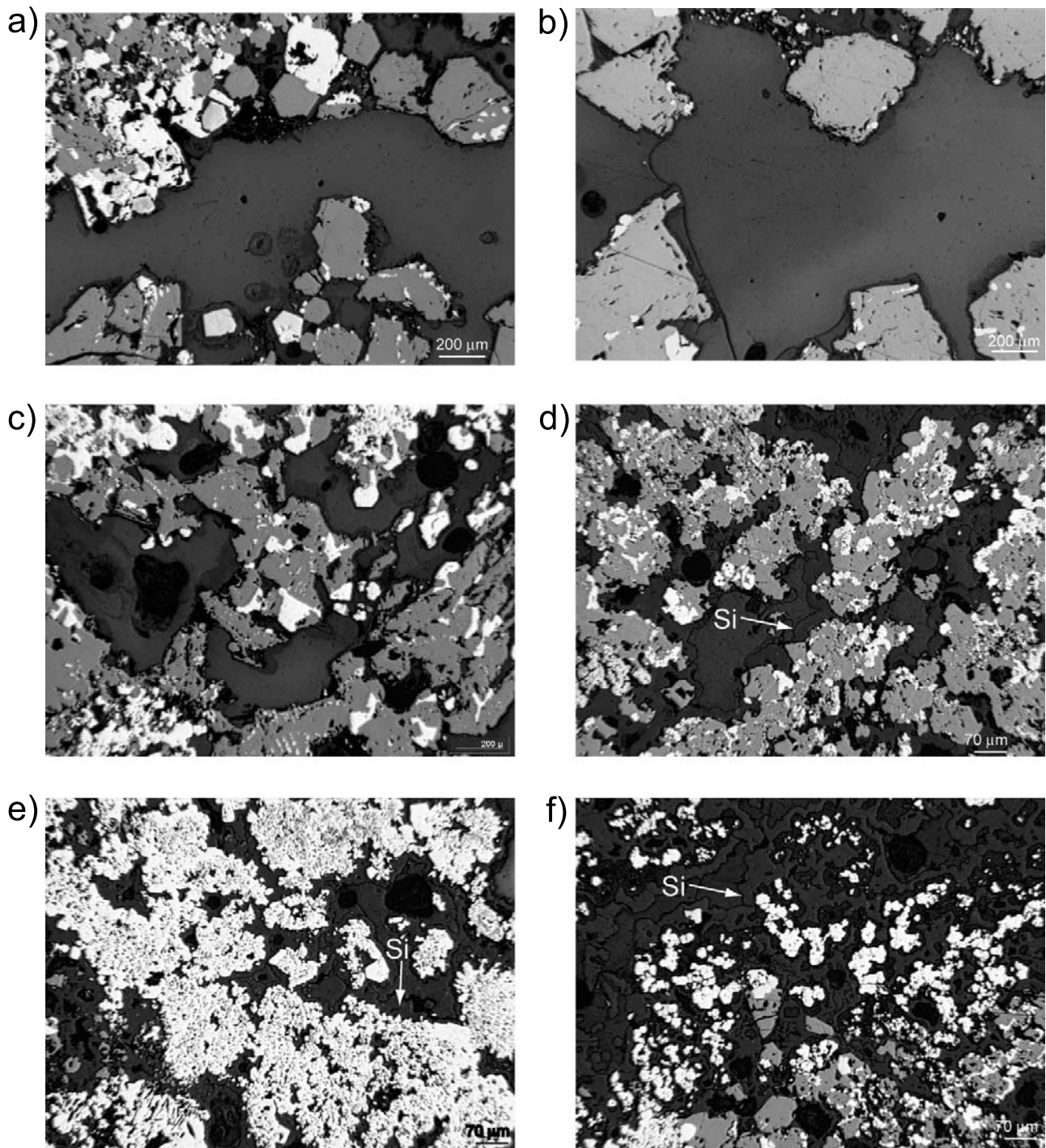
Figure 7. Photomicrographs (reflected light) from interior portions of Phang where there is a heterogeneous distribution of amorphous silica. Amorphous silica is absent or present in only trace amounts along porous, linearly continuous sections as shown in core 1A2_#7 (a–b) and 1A2_3#8 (c). In areas with increasing distance from the amorphous silica-free zones, mineral composition differs, with greater amounts of pyrite and amorphous silica (as a late stage coating) present as shown in cores 1A2_#7 (d) and 1A2_3#8 (e–f). Minerals shown are wurtzite (light gray), pyrite or chalcopyrite (white), and amorphous silica (Si) (dark gray). Void space (epoxy filled) also appears dark gray in reflected light.

(Figure 4) are not without ambiguity. However, we argue here that the groupings we propose are evident, at least for the Roane structure, in the spatial position of cores within the vent structure. For cores from Roane, data that define

the steeper trend ($k \propto \phi^9$) are for cores that were all taken from the inner portion of the spire, within 14 cm of its axis, whereas data that define the shallower trend ($k \propto \phi^3$) are for cores taken from the outer portion of the spire, greater than
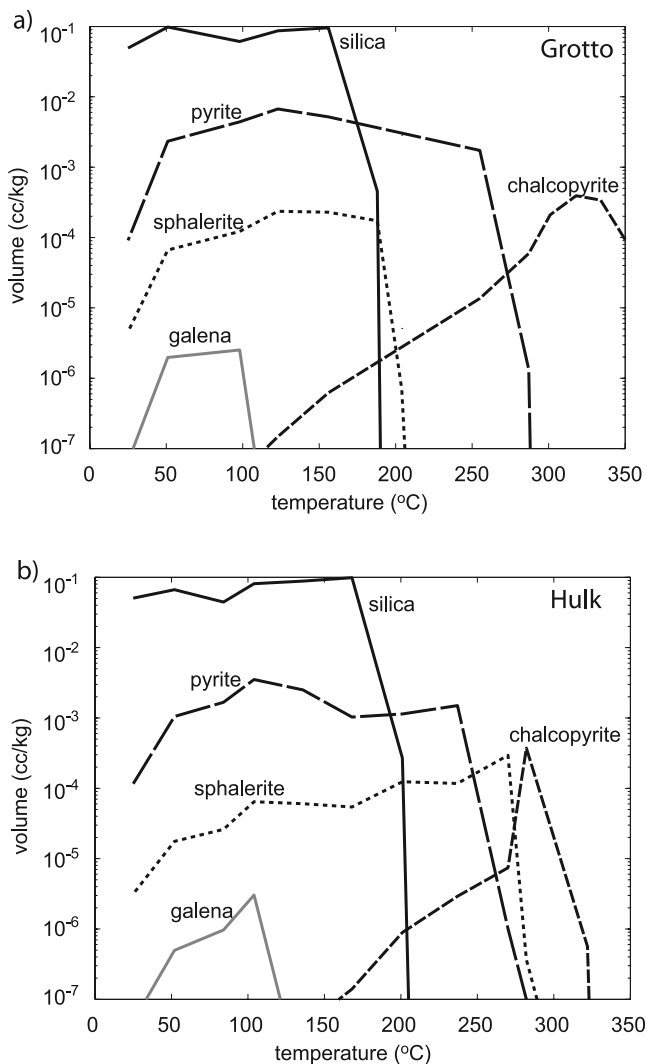
Figure 8. Volumes (in cc/kg fluid) of solids precipitated as a function of temperature during cooling of MEF (a) Grotto and (b) Hulk vent fluids (see *Tivey et al.* [1999] for details of fluid composition used in calculations; after *Butterfield et al.* [1994] and *Lilley et al.* [1993]). Calculations were carried out using the computer program EQ3/6 [*Wolery*, 1992a, 1992b; *Wolery and Daveler*, 1992], assuming an open system equilibrium model, with minerals transferred after precipitation; no back reaction was allowed. Differences in mineral saturation as a function of temperature reflect differences in concentrations of certain elements and also differences in pH. For example, Hulk vent fluid has lower concentrations of Zn, Fe, and H_2S, and a higher concentration of Si, than Grotto vent fluid, resulting in differences in the temperatures at which chalcopyrite, pyrite, and amorphous silica are predicted to precipitate. Hulk vent fluid, however, also exhibits a higher pH at any given temperature than Grotto vent fluid, resulting in the prediction that sphalerite will precipitate from Hulk vent fluid at a significantly higher temperature despite lower concentrations of Zn and H_2S. Precipitation of quartz, chalcedony, cristobalite, and coesite was suppressed during calculations; see text for description of the thermodynamic database used in calculations.

14 cm from the spire's axis. Observations of mineral composition and texture for each core further support our separation of these two groups. For all three vent structures the steeper trend corresponds to cores that exhibit greater amounts of sulfide than amorphous silica, and when amorphous silica is present in the core, its distribution is patchy and it is absent or present only as a trace phase along porous, linearly continuous sections that are composed dominantly of pore space, wurtzite/sphalerite, and chalcopyrite and/or pyrite (Figures 5, 6a–6c, and 7a–7c). In Finn, all cores are group I cores (Figure 4c) and have only minor to trace amounts of amorphous silica. Sulfide minerals present range in size from 30 to >250 μm and are anhedral to euhedral. In Roane group I cores, amorphous silica is absent in many parts of the cores, and when present is as a very thin (<10 μm) discontinuous layer on clay and less commonly on sulfide (Figures 6a–6c). Sulfide grain size varies from 50 to >250 μm and grains are anhedral to euhedral. In Phang, while there is amorphous silica present in group I cores, it is present in only minor quantities or is absent along what were likely the dominant flow paths: porous, linearly continuous sections that are composed dominantly of pore space, wurtzite, chalcopyrite and pyrite (Figures 5 and 7a–7c). Anhedral to euhedral sulfide grains average 30 to 150 μm in size. This mineral assemblage likely formed from high-temperature fluids (200–300°C). In a detailed study of the mineralogy, texture and geochemistry of the structure Roane, *Kristall et al.* [2006] identified Zn sulfides (wurtzite and/or sphalerite) + chalcopyrite as the highest-temperature mineral assemblage, resulting from high-temperature flow through the central zone composed of Zn sulfide and pyrite. Thus this steeper trend in permeability-porosity data corresponds to environments where porosity is changing (decreasing) as a result of deposition of sulfide minerals, and this evolution of porosity is resulting in a dramatic decrease in permeability. The precipitation of angular sulfide minerals blocks fluid flow passages effectively, causing significant pore connectivity loss (e.g., Figure 6c).

[20] For both Roane and Phang, the shallower permeability-porosity trend corresponds to cores that have a greater abundance of amorphous silica than sulfide. No cores taken from Finn, which only exhibits only minor to trace amorphous silica, plot on this shallower trend. In both Roane and Phang group II cores, amorphous silica is present throughout the core (except in isolated wurtzite-rich patches) as a 30 to 150 μm coating. In these cores porosity decrease is the result of deposition of successive thin layers of amorphous silica along all surfaces. The presence of amorphous silica-rich textures is consistent with formation from lower temperature, conductively cooled fluid [e.g., *Tivey and Delaney*, 1986]. As a gel coat, amorphous silica doesn't block fluid flow passages as effectively; instead the coating continuously reduces the pore size. While both precipitation processes cause porosity loss, sulfide deposition is more effective in blocking fluid flow and thus causes more drastic permeability reduction, whereas amorphous silica deposition causes a more gradual permeability loss. Note that in Figures 4a and 4b, the two trends converge at low porosity (<15%). This is likely because void space is reduced below the pinch-off threshold (where pore connectivity loss

occurs) during the continuous amorphous silica precipitation [*Zhu et al.*, 1995].

[21] The thermodynamic calculations that consider cooling of vent fluid support the interpretation that the sulfide dominated textures reflect formation from higher-temperature fluids, while the presence of amorphous silica indicates significant cooling of the vent fluid (Figure 8). The calculations predict assemblages of chalcopyrite, pyrite, and sphalerite at temperatures of ~200°C, and assemblages of chalcopyrite and pyrite and/or sphalerite at higher temperatures. The calculated precipitation temperatures for pyrite and chalcopyrite fit well with observations of *Kristall et al.* [2006], but the low calculated temperature for precipitation of Zn sulfide, particularly from Grotto fluid, does not. *Kristall et al.* [2006] present evidence that wurtzite ± sphalerite precipitated in the hottest areas of the Roane structure at temperatures likely close to 300°C. The failure of calculations to reproduce this observation likely results from discrepancies related to three factors: calculated pH, vent fluid metal concentrations, and thermodynamic data for Zn sulfide minerals (sphalerite and wurtzite) and Zn chloride complexes. The solubility of sphalerite is strongly pH dependent; for the same concentrations of Zn and H_2S, a higher pH would result in saturation of sphalerite at a higher temperature [e.g., *Tivey et al.*, 1999]. For example, the prediction that sphalerite is saturated at higher temperatures with cooling of Hulk versus Grotto fluid is a result of the higher pH of Hulk fluid; Grotto fluid is in fact enriched in Zn and H_2S relative to Hulk fluid (35 versus 32 μmol/kg Zn and 6.2 versus 2.9 mmol/kg H_2S). *Kristall et al.* [2006] note that the pH (25°C) for Mothra fluids is 4.7 to 4.8, significantly higher than the values of 4.5 and 4.2 used in calculations for Hulk and Grotto vent fluid, respectively. Similarly, sphalerite would be predicted to be saturated at higher temperatures if concentrations of Zn or H_2S in Mothra fluids were greater than those in the fluid compositions used in calculations. Finally, thermodynamic calculations using the SUPCRT92 database and additions as described have been shown previously to fail in reproducing the presence of Zn sulfide phases in vent deposits. *Tivey* [1995] noted the likelihood that this reflects incorrect thermodynamic data for the $ZnCl^+$ complex, which is likely too strong, resulting in a lower effective Zn concentration. Use of data for sphalerite, instead of the metastable polymorph wurtzite that dominates the Roane and Phang mineral assemblages, would also result in a lower predicted temperature of saturation, though would have a less significant effect than the effect of the overly strong $ZnCl^+$ complex [*Tivey*, 1995]. If the calculations were done assuming a higher pH (25°C), with higher Zn concentrations, using a weaker $ZnCl^+$ complex and data for wurtzite instead of sphalerite, then the predicted temperature for precipitation of Zn sulfide would be closer to the 300°C predicted on the basis of mineral texture and geochemistry. The thermodynamic calculations of cooling also show that amorphous silica is saturated by ~200°C, and is the dominant phase precipitating at temperatures of 150°C and lower. These calculations indicate that fluids that cool conductively and precipitate sulfide minerals as they cool will become saturated in amorphous silica, resulting in precipitation of dominantly amorphous silica at temperatures of 150°C and less.

[22] These results help explain observations in the Roane and Phang group I and group II cores. In Roane group I cores, vol% sulfide and pore space are inversely correlated and amorphous silica is present in only small amounts. These cores were taken from the inner 14 cm of Roane. Thus at the time that Roane was recovered, its central part was likely at temperatures greater than 150°C. Hot fluids transited through this central core, most exiting the top, some exiting through the sides. These portions of the structure are composed of sulfide and pore space, and sulfide was precipitating along flow paths [*Kristall et al.*, 2006]. At the time of Roane's recovery, the temperature of fluid exiting the top of Roane was 169°C, with cooler fluids (ca. 80°C) exiting the sides [*Kristall et al.*, 2006]. *Kristall et al.* [2006] also note that 278°C is a minimum estimate for the temperatures of fluids feeding the base of Roane, based on temperatures from instrumented drill holes within Roane's base (up to 278°C) and from two nearby chimneys (up to 300°C). In Phang group I cores, vol% sulfide and pore space are not inversely correlated. Instead vol% sulfide and vol% amorphous silica are inversely correlated. This reflects deposition of amorphous silica in significant amounts of pore space even within group I cores. However, this amorphous silica is present in only minor quantities or is absent along what were likely the dominant flow paths: the porous, linearly continuous sections that are composed dominantly of pore space and the highest-temperature mineral assemblage of wurtzite, chalcopyrite and pyrite (Figures 7a–7c). On the basis of the texture and mineral composition, these portions of the sample are interpreted to be relic flow channels for highest-temperature fluids within the structure when it was last active. In other parts of the Phang group I cores, where there are greater amounts of pyrite, lesser amounts of chalcopyrite, and at increasing distance from the porous, linearly continuous sections, amorphous silica is present as a continuous thick coating (30–150 μm; Figures 7d–7f). These silica-rich areas likely resulted from percolation of fluids outward from the main flow channels into dead-end minor conduits (e.g., into noneffective porosity). Cooling of the fluids in these dead-end conduits would result in deposition of silica, as shown by the thermodynamic calculations (Figure 8).

[23] In contrast to the group I cores, the dominant process resulting in permeability decrease in group II cores is amorphous silica precipitation, as a coating on existing pyrite/wurtzite grains (Figures 6d–6f). For both Roane and Phang, there is an inverse correlation of vol% sulfide and vol% amorphous silica in group II cores. The Roane group II cores were all obtained from the outer parts of the structure, where temperatures were cooler. Some of the hot fluids in Roane's interior were thus transiting across the outer portions and cooling. As the fluids cooled, amorphous silica became saturated and precipitated, decreasing pore space. The cooling was also likely enhanced by slower flow rates (note that all amorphous silica-rich cores have permeabilities $<2 \times 10^{-14}$ m^2).

5.2. Permeability-Porosity Relationships

[24] While laboratory data on permeability-porosity relationships of deep-sea hydrothermal vent deposits are limited, the evolution of permeability and porosity of sedimentary rocks during various geological processes has been inves-

tigated, because of its importance in reservoir and petroleum engineering. Theoretical analyses and laboratory measurements carried out on various rock and sediment types support a generalized power law relationship ($k \propto \phi^{\alpha}$) [e.g., *Paterson*, 1983; *Walsh and Brace*, 1984; *David et al.*, 1994; *Wark and Watson*, 1998; *Zhu et al.*, 1999]. The power law exponent α is sensitive both to materials and to evolution processes (e.g., processes that change pore space through time, such as compaction, deformation, precipitation, dissolution).

[25] In seafloor vent deposit samples the primary pore evolution process is mineral deposition (and in some portions of samples minor amounts of mineral dissolution, and thermal cracking). *Bernabé et al.* [2003] provide an excellent summary of values of α for different processes and materials. Some of the processes pertinent for seafloor vent deposits include (1) physical processes, such as crack opening due to thermal stress, $\alpha = 5$ to 7 in dense rocks; and (2) chemical processes, such as precipitation: $\alpha \approx 8$ in sedimentary rocks, $\alpha = 4.5$ for sintering in porous glass, $\alpha \approx 2$ for diagenesis at porosities <0.10, and dissolution: $\alpha > 20$ in sedimentary rocks. While studies have not been done that consider precipitation of sulfide versus amorphous silica, studies have been done that consider changes in permeability-porosity relationships with precipitation of gypsum and quartz.

[26] *Reis and Acock* [1994] showed a power law permeability-porosity relationship with an exponent of ~8 when supersaturated fluids precipitate gypsum and quartz in Berea sandstone samples. The result is similar to our data for group I cores during sulfide/sulfate precipitation. In another study, *Bourbié and Zinszner* [1985] showed a permeability-porosity relationship with an exponent of ~3 in a suite of natural Fontainebleau sandstone samples with different degrees of cementation. Previous studies show that in Fontainebleau sandstone, various amount of quartz cement precipitate in the pore space, partially or completely coating original quartz grains [*Bourbié and Zinszner*, 1985]. Cathodoluminescence images of this late stage cement in Fontainebleau sandstones document several thin bands of silica, deposited either as amorphous or poorly crystalline silica (as in the Phang and Roane cores) or poorly crystalline to crystalline quartz [*Haddad et al.*, 2006]. Thus the process of pore evolution (porosity decrease from deposition of thin layers of silica cement) and the exponent of ~3 are similar for our group II cores and for cementation in Fontainebleu sandstone. Notwithstanding the uncertainties in our permeability measurements (Figure 4, especially for Phang cores where there is a lack of cores with relatively high porosities), the similarity between the pore evolution processes in Fontainebleau sandstone and our group II cores supports our interpretation that there exist two different permeability-porosity trends, with an exponent of ~3 for group II cores. In both cases, the similarity in permeability-porosity relationships can be explained by the similarity in the evolution of pore space. These results suggest that correct identification of pore space evolution processes is the key to successfully relating permeability to porosity.

5.3. Insights Into Vent Structure Evolution

[27] Our data on Mothra hydrothermal vent structures suggest that the differences in α of EPPRs, determined from measurements of permeability on the small scale (cm to tens of cm) are relevant to flow in vent structures, and provide important information about fluid flow and vent structure evolution in active seafloor deposits. For example, data obtained from the Roane and Phang cores show that for silica-free, sulfide/sulfate dominated structures, a decrease in porosity from 25% to 15% via sulfide/sulfate deposition will result in a nearly two orders of magnitude decrease in permeability, and a similar decrease in flow rate (assuming a constant pressure gradient, since then volumetric flow rate Q is directly proportional to permeability k). A consequence of this is that biological communities residing on the surfaces of these structures would need strategies for dealing with these rapidly decreasing flow rates. In contrast, for vent sites where amorphous silica deposition is prevalent (e.g., along the Endeavour segment, JFR) the same porosity change from deposition of amorphous silica would result in less than an order of magnitude decrease in permeability, and, assuming a constant pressure gradient, less than an order of magnitude change in flow rate. On the basis of these observations, a conceptual model of the evolution of EPPRs in vent deposits is given in Figure 9. Our hypothesis on the course of chimney growth at the Mothra hydrothermal vent site is that at relatively high temperatures with more vigorous flow, and higher throughput of fluid, sulfide deposition dominates the evolution of pore structure. Sulfide deposition causes the loss of pore connectivity and thus drastically reduces permeability and therefore impedes fluid flow. As flow rate drops and temperature cools, amorphous silica precipitation gains more control over the evolution of pore structure in the vent deposits. It is conceivable that once the flow rate drops below a certain threshold, sulfide/sulfate deposition will be negligible. For example, on the basis of thermodynamic calculations, if flow rates drop so low that fluids have time to cool conductively to 150°C or less, then amorphous silica deposition would dominate. In contrast to sulfide deposition, amorphous silica precipitation reduces permeability gradually and likely results in a quasi-steady state of fluid circulation. This may contribute to the observations that lush biological communities are present on the exteriors of the diffusing spires.

[28] Our results also provide insight into how the Mothra structures evolve. Our data suggest that there is a feedback from mineral deposition within Mothra structures that leads to greater homogeneity and thus less channeled and more diffuse flow as these spires age. Greater flow through more permeable sections of the structures results in higher temperatures and deposition of sulfide, decreasing permeability at a greater rate than in portions with lower permeability. Lower flow rates, lower temperatures, and deposition of amorphous silica, which would not decrease permeability as much for a given porosity decrease, dominates in the less permeable sections of the structures. That the diffusing spire structures become more homogeneous with respect to permeability over time is supported by our portable permeameter results, which demonstrate that the mean permeability of the inactive structure Phang is less than of Roane, as is the standard deviation of permeability values. Thus our measurements, and identification of other EPPRs relevant to hydrothermal vent systems, can aid in predicting deposit evolution and whether cascading feedbacks likely lead to
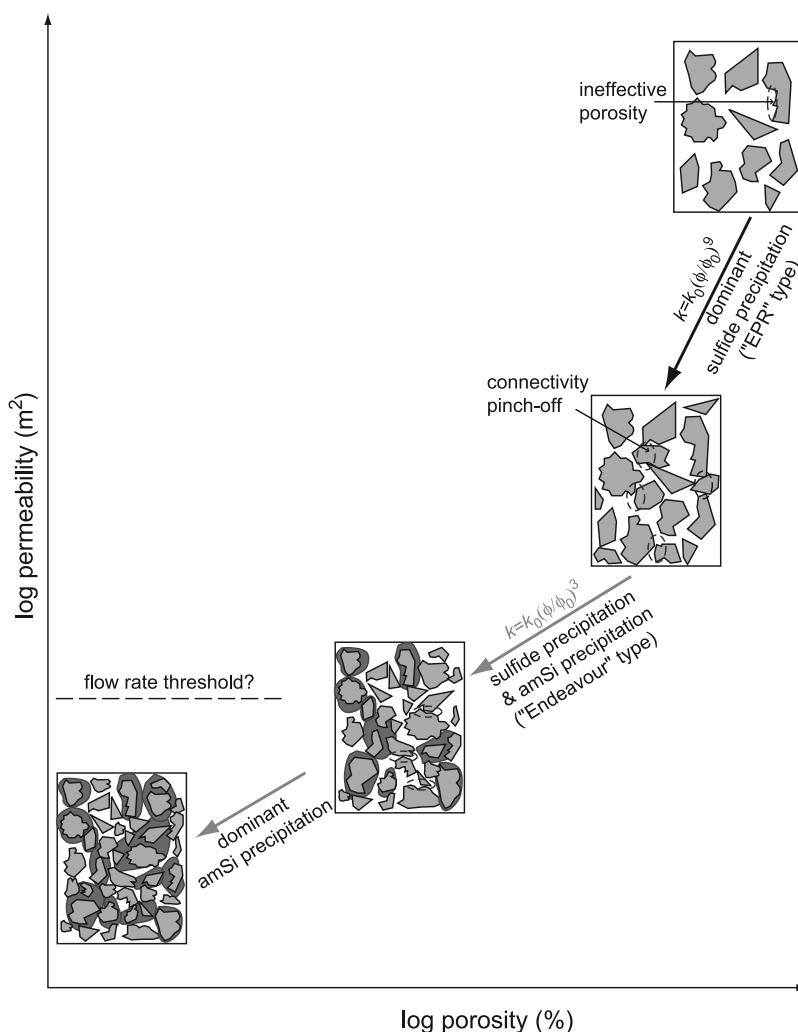
Figure 9. Working hypothesis of the evolution of permeability-porosity relationships in vent deposits at the Mothra Hydrothermal field.

clogging of flow paths, or whether feedback is such that fluid flow is maintained in certain portions of structures.

6. Conclusions

[29] Measurements made on large blocks of seafloor vent structures show permeability values of 10^{-16} to 10^{-11} m^2 that correlate strongly with different textures. Our data show that the mean permeability value of the low-temperature diffuse spire Roane is comparable to that of the black smoker Finn. However, the currently inactive spire Phang has a mean permeability value approximately a half order of magnitude lower than that of Roane or Finn. More quantitative measurements of axial permeabilities yield values ranging from $\sim 10^{-15}$ to 10^{-13} m^2 for cores from an inactive chimney, $\sim 10^{-15}$ to 10^{-12} m^2 for cores from an active chimney exhibiting diffuse flow, and $\sim 10^{-15}$ to 3×10^{-13} m^2 for cores of a thick black smoker wall. Our data document two distinct trends in relations of permeability to porosity. A power law with an exponent of ~ 9 best describes the data from portions of the chimneys where sulfide precipitation is the dominant process affecting pore structure, and a power law with an exponent of ~ 3 best

describes the relation between permeability and porosity where amorphous silica is present as a late stage precipitate filling pore space. Microstructural observations suggest that the difference in the two permeability-porosity relationships reflects different pore evolution processes, as pores are sealed either with angular sulfide grains, or by late stage amorphous silica. While the former tends to nucleate as single large crystals or as aggregates that block fluid paths very efficiently, the latter tends to precipitate as a thin coating on existing grains, which reduces fluid pathways more gradually.

[30] These data document the close relationship between transport properties and vent growth processes. For example, the identified relationships lead to the prediction that the permeability of Mothra structures becomes more homogeneous over time, resulting in less focused and more diffuse flow. In addition, during deposition of amorphous silica, rates of fluid flow will be more constant, and permeability will decrease less rapidly for a given change in porosity, such as in exterior portions of structures within Endeavour segment vent fields (e.g., at Mothra, MEF, and the High-Rise field). These are locations where lush biological communities are common [Delaney et al., 1992;

Robigou et al., 1993; *Kelley et al.*, 2001]. Laboratory measurements of transport properties thus provide a useful tool for understanding the interactions among hydrothermal fluid, seawater, solid substrates, and biological organisms.

[31] Observations of vent deposits from many sites on the mid-Atlantic Ridge, East Pacific Rise, and JFR indicate common textural features in similar types of vent deposits, e.g., in high-temperature concentric black smoker chimneys, lower-temperature (<300°C) zinc-rich chimneys, and in flanges [e.g., *Haymon and Kastner*, 1981; *Goldfarb*, 1988; *Haymon*, 1983; *Koski et al.*, 1984, 1994; *Hannington et al.*, 1995; *Paradis et al.*, 1988; *Fouquet et al.*, 1993; *Tivey et al.*, 1995, 1999]. It is not surprising that there appear to be porosity and porosity structure (and thus possibly permeability) relationships common to specific textures and sample types. This reflects that these deposits form in a common way, as a result of precipitation of minerals from aqueous solutions. Thus we believe it likely that permeability/porosity structure relationships can be developed for distinct textures of these different vent deposit types, and that these relationships will be able to be applied to similar deposit types from numerous seafloor vent sites to better understand how vent deposits evolve, and the dynamics of fluid flow and environmental conditions within the deposits as a function of their evolution. Our data suggest that correctly identifying the processes of pore space evolution in seafloor vent deposits is the key to successfully relating permeability to porosity.

References

Bernabé, Y., U. Mok, and B. Evans (2003), Permeability-porosity relationships in rocks subjected to various evolution processes, *Pure Appl. Geophys.*, 160(5–6), 937–960.

Bourbié, T., and B. Zinszner (1985), Hydraulic and acoustic properties as a function of porosity in Fontainebleau sandstone, *J. Geophys. Res.*, 90, 11,524–11,532.

Bowers, T. S., K. L. Von Damm, and J. M. Edmond (1985), Chemical evolution of mid-ocean ridge hot springs, *Geochim. Cosmochim. Acta*, 49, 2239–2252.

Butterfield, D. A., R. E. McDuff, M. J. Mottl, M. D. Lilley, J. E. Lupton, and G. J. Massoth (1994), Gradients in the composition of hydrothermal fluids from the Endeavour segment vent field: Phase separation and brine loss, *J. Geophys. Res.*, 99, 9561–9583.

Cary, S. C., T. Shank, and J. Stein (1998), Worms bask in extreme temperatures, *Nature*, 391, 545–546.

David, C., T.-f. Wong, W. Zhu, and J. Zhang (1994), Laboratory measurement of compaction-induced permeability change in porous rocks: Implications for the generation and maintenance of pore pressure excess in the crust, *Pure Appl. Geophys.*, 143, 425–456.

Delaney, J. R., V. Robigou, R. E. McDuff, and M. K. Tivey (1992), Geology of a vigorous hydrothermal system on the Endeavour segment, Juan de Fuca Ridge, *J. Geophys. Res.*, 97, 19,663–19,682.

Delaney, J. R., D. S. Kelley, E. A. Mathez, D. R. Yoerger, J. Baross, M. Schrenk, M. K. Tivey, J. Kaye, and V. Robigou (2001), "Edifice Rex" sulfide recovery project: Analysis of a submarine microbial habitat, *EOS Trans. AGU*, 82, 67–73.

Ding, K., and W. E. Seyfried Jr. (1992a), Determination of Fe-Cl complexing in the low pressure supercritical region (NaCl fluid): Iron solubility constraints on pH of subseafloor hydrothermal fluids, *Geochim. Cosmochim. Acta*, 56, 3681–3692.

Ding, K., and W. E. Seyfried Jr. (1992b), Experimental determination of Cu-Cl speciation at the T-P conditions relevant to ridge crest hydrothermal activity: Implications to log (fO$_2$) in the hot spring fluids (abstract), *Eos Trans. AGU*, 73(43), Fall Meeting Suppl., 254.

Edmond, J. M., A. C. Campbell, M. R. Palmer, C. R. German, G. P. Klinkhammer, H. N. Edmonds, H. Elderfield, G. Thompson, and P. Rona (1995), Time series studies of vent fluids from the TAG and MARK sites (1986, 1990) mid-Atlantic Ridge and a mechanism for Cu/Zn zonation in massive sulphide ore bodies, in *Hydrothermal Vents and Processes*, edited by L. M. Parson et al., Spec. Publ. Geol. Soc. London, 87, 77–86.

Fouquet, Y., A. Wafik, P. Cambon, C. Mével, G. Meyer, and P. Gente (1993), Tectonic setting and mineralogical and geochemical zonation in the Snake Pit sulfide deposit (Mid-Atlantic Ridge at 23°N), *Econ. Geol.*, 88, 2018–2036.

Goldfarb, M. S. (1988), Flanges and the formation of hydrothermal edifices, Endeavour segment, Juan de Fuca Ridge (abstract), *Eos Trans. AGU*, 69(44), Fall Meeting Suppl., 1484.

Goldfarb, M. S., D. R. Converse, H. D. Holland, and J. M. Edmond (1983), The genesis of hot spring deposits on the East Pacific Rise, 21°N, *Econ. Geol. Monogr.*, 5, 184–197.

Haddad, S. C., R. H. Worden, D. J. Prior, and P. C. Smalley (2006), Quartz cement in the Fontainebleau sandstone, Paris Basin, France: Crystallography and implications for mechanisms of cement growth, *J. Sediment. Res.*, 76, 244–256, doi:10.2110/jsr.2006.024.

Hannington, M. D., and S. D. Scott (1988), Mineralogy and geochemistry of a hydrothermal silica-sulfide-sulfate spire in the caldera of Axial Seamount, Juan de Fuca Ridge, *Can. Mineral.*, 26, 603–625.

Hannington, M. D., I. R. Jonasson, P. M. Herzig, and S. Petersen (1995), Physical and chemical processes of seafloor mineralization at mid-ocean ridges, in *Seafloor Hydrothermal Systems: Physical, Chemical, Biological, and Geological Interactions*, Geophys. Monogr. Ser., vol. 91, edited by S. E. Humphris et al., pp. 115–157, AGU, Washington, D. C.

Haymon, R. (1983), Growth history of hydrothermal black smoker chimneys, *Nature*, 301, 695–698.

Haymon, R. M., and M. Kastner (1981), Hot spring deposits on the East Pacific Rise at 21°N: Preliminary description of mineralogy and genesis, *Earth Planet. Sci. Lett.*, 53, 363–381.

Haymon, R. M., R. A. Koski, and C. Sinclair (1984), Fossils of hydrothermal vent worms from Cretaceous sulfide ores of the Samail Ophiolite, Oman, *Science*, 223, 1407–1409.

Janecky, D. R., and W. E. Seyfried Jr. (1984), Formation of massive sulfide deposits on oceanic ridge crests: Incremental reaction models for mixing between hydrothermal solutions and seawater, *Geochim. Cosmochim. Acta*, 48, 2723–2738.

Janecky, D. R., and W. C Shanks III (1988), Computational modeling of chemical and sulfur isotopic reaction processes in seafloor hydrothermal systems: Chimneys, massive sulfides, and subjacent alteration zones, *Can. Mineral.*, 26, 805–825.

Johnson, J. W., E. H. Oelkers, and H. C. Helgeson (1992), SUPCRT92: A software package for calculating the standard molal thermodynamic properties of minerals, gases, aqueous species, and reactions from 1–5000 bars and 0–1000°C, *Comput. Geosci.*, 18, 899–947.

Juniper, S. K., I. R. Jonasson, V. Tunnicliffe, and A. J. Southward (1992), Influence of a tube-building polychaete on hydrothermal chimney mineralization, *Geology*, 20, 895–898.

Kelley, D. S., J. R. Delaney, and D. R. Yoerger (2001), Geology and venting characteristics of the Mothra hydrothermal field, Endeavour segment, Juan de Fuca Ridge, *Geology*, 29, 959–962, doi:10.1130/0091-7613.

Koski, R. A. (1987), Sulfide deposits on the seafloor: Geological models and resource perspectives based on studies in ophiolite sequences, in *Marine Minerals, Resource Assessment Strategies*, Proc. NATO Adv. Res. Workshop, Ser. C, vol. 194, edited by P. G. Teleki et al., pp. 301–316, Springer, New York.

Koski, R. A., D. A. Clague, and E. Oudin (1984), Mineralogy and chemistry of massive sulfide deposits from the Juan de Fuca Ridge, *Geol. Soc. Am. Bull.*, 95, 930–945.

Koski, R. A., I. R. Jonasson, D. C. Kadko, V. K. Smith, and F. L. Wong (1994), Compositions, growth mechanisms, and temporal relations of hydrothermal sulfide-sulfate-silica chimneys at the northern Cleft segment, Juan de Fuca Ridge, *J. Geophys. Res.*, 99, 4813–4832.

Kristall, B., D. S. Kelley, M. D. Hannington, and J. R. Delaney (2006), Growth history of a diffusely venting sulfide structure from the Juan de Fuca Ridge: A petrological and geochemical study, *Geochem. Geophys. Geosyst.*, 7, Q07001, doi:10.1029/2005GC001166.

Le Bris, N., M. Zbinden, and F. Gaill (2005), Processes controlling the physicochemical micro-environments associated with Pompeii worms, *Deep Sea Res., Part I*, 52, 1071–1083.

Lilley, M. D., D. A. Butterfield, E. J. Olson, J. E. Lupton, S. A. Macko, and R. E. McDuff (1993), Anomalous CH$_4$ and NH4$^+$ concentrations at an unsedimented mid-ocean-ridge hydrothermal system, *Nature*, 364, 45–47.

Luther, G. W., T. F. Rozan, M. Taillefert, D. B. Nuzzio, C. D. Meo, T. M. Shank, R. A. Lutz, and S. C. Cary (2001), Chemical speciation drives hydrothermal vent ecology, *Nature*, *410*, 813–816.

McCollom, T. M., and E. L. Shock (1997), Geochemical constraints on chemolithoautotrophic metabolism by microorganisms in seafloor hydrothermal systems, *Geochim. Cosmochim. Acta*, *61*, 4375–4391.

Oudin, E. (1983), Mineralogie de gisements et indices lies a des zones d'accretionoceaniques actuelles (ride Est Pacific et Mer Rouge) et fossile (Cyphere), *Chron. Rech. Min.*, *470*, 43–55.

Oudin, E., and G. Constantinou (1984), Black smoker chimney fragments in Cyprus sulphide deposits, *Nature*, *308*, 349–353.

Paradis, S., I. R. Jonasson, G. M. Le Cheminant, and D. H. Watkinson (1988), Two zinc-rich chimneys from the Plume Site, southern Juan de Fuca Ridge, *Can. Mineral.*, *26*, 637–654.

Paterson, M. S. (1983), The equivalent channel model for permeability and resistivity in fluid-saturated rock: A re-appraisal, *Mech. Mater.*, *2*, 345–352.

Reis, J. C., and A. M. Acock (1994), Permeability reduction models for the precipitation of inorganic solids in Berea sandstone, *In Situ*, *18*, 347–368.

Robigou, V., J. R. Delaney, and D. S. Stakes (1993), Large massive sulfide deposits in a newly discovered active hydrothermal system, the High-Rise field, Endeavour segment, Juan de Fuca Ridge, *Geophys. Res. Lett.*, *20*(17), 1887–1890.

Sarrazin, J., C. Levesque, S. K. Juniper, and M. Tivey (2002), Mosaic community dynamics on Juan de Fuca Ridge sulfide edifices: Substratum, temperature and implications for trophic structure, *Cah. Biol. Mar.*, *43*, 275–279.

Shock, E. L., and M. E. Holland (2004), Geochemical energy sources that support the subsurface biosphere, in *Subseafloor Biosphere at Mid-Ocean Ridges*, *Geophys. Monogr. Ser.*, vol. 144, edited by W. Wilcock et al., pp. 153–165, AGU, Washington, D. C.

Sutherland, W. J., C. Halvorsen, A. Hurst, C. A. McPhee, G. Robertson, P. R. Whattler, and P. F. Worthington (1993), Recommended practice for probe permeametry, *Mar. Pet. Geol.*, *10*, 309–317.

Sverjensky, D. A., J. J. Hemley, and W. M. d'Angelo (1991), Thermodynamic assessment of hydrothermal alkali feldspar-mica-aluminosilicate equilibria, *Geochim. Cosmochim. Acta*, *4*, 989–1004.

Tivey, M. K. (1995), The influence of hydrothermal fluid composition and advection rates on black smoker chimney mineralogy: Insights from modeling non-reactive transport, *Geochim. Cosmochim. Acta*, *59*, 1933–1949.

Tivey, M. K. (2004), Environmental conditions within active seafloor vent structures: Sensitivity to vent fluid composition and fluid flow, in *Subseafloor Biosphere at Mid-Ocean Ridges*, *Geophys. Monogr. Ser.*, vol. 144, edited by W. Wilcock et al., pp. 137–152, AGU, Washington, D. C.

Tivey, M. K., and J. R. Delaney (1986), Growth of large sulfide structures on the Endeavour segment of the Juan de Fuca Ridge, *Earth Planet. Sci. Lett.*, *77*, 303–317.

Tivey, M. K., and R. E. McDuff (1990), Mineral precipitation in the walls of black smoker chimneys: A quantitative model of transport and chemical reaction, *J. Geophys. Res.*, *95*, 12,617–12,637.

Tivey, M. K., S. E. Humphris, G. Thompson, M. D. Hannington, and P. Rona (1995), Deducing patterns of fluid flow and mixing within the active TAG hydrothermal mound using mineralogical and geochemical data, *J. Geophys. Res.*, *100*, 12,527–12,555.

Tivey, M. K., D. S. Stakes, T. L. Cook, M. D. Hannington, and S. Petersen (1999), A model for growth of steep-sided vent structures on the Endeavour segment of the Juan de Fuca Ridge: Results of a petrologic and geochemical study, *J. Geophys. Res.*, *104*, 22,859–22,883.

Walsh, J. B. (1965), The effect of cracks on the compressibility of rock, *J. Geophys. Res.*, *70*, 381–389.

Walsh, J. B., and W. F. Brace (1984), The effect of pressure on porosity and the transport properties of rock, *J. Geophys. Res.*, *89*, 9425–9431.

Wark, D. A., and E. B. Watson (1998), Grain-scale permeabilities of texturally equilibrated, monomineralic rocks, *Earth Planet. Sci. Lett.*, *164*, 591–605.

Wolery, T. J. (1992a), *EQ3NR, A Computer Program for Geochemical Aqueous Speciation-Solubility Calculations: Theoretical Manual, User's Guide, and Related Documentation (Version 7.0)*, Lawrence Livermore Natl. Lab., Livermore, Calif.

Wolery, T. J. (1992b), *EQ3/6, A Software Package for Geochemical Modeling of Aqueous Systems: Package Overview and Installation Guide (Version 7.0)*, Lawrence Livermore Natl. Lab., Livermore, Calif.

Wolery, T. J., and S. A. Daveler (1992), *EQ6, A Computer Program for Reaction Path Modeling of Aqueous Geochemical Systems: Theoretical Manual, User's Guide, and Related Documentation (Version 7.0)*, Lawrence Livermore Natl. Lab., Livermore, Calif.

Woods, A. W., and J. R. Delaney (1992), The heat and fluid transfer associated with the flanges on hydrothermal venting structures, *Earth Planet. Sci. Lett.*, *112*, 117–129.

Zhu, W., C. David, and T.-f. Wong (1995), Network modeling of permeability evolution during cementation and hot isostatic pressing, *J. Geophys. Res.*, *100*, 15,451–15,464.

Zhu, W., B. Evans, and Y. Bernabé (1999), Densification and permeability reduction in hot-pressed calcite: A kinetic model, *J. Geophys. Res.*, *104*, 25,501–25,511.

————————————

P. R. Craddock, Department of Marine Chemistry and Geochemistry, WHOI, Woods Hole, MA 02543, USA.

H. Gittings, Department of Geology and Geophysics, University of Wisconsin-Madison, 1215 West Dayton Street, Madison, WI 53706, USA.

M. K. Tivey, Department of Marine Chemistry and Geochemistry, WHOI, Woods Hole, MA 02543, USA.

W. Zhu, Department of Geology and Geophysics, WHOI, Woods Hole, MA 02543, USA. (wzhu@whoi.edu)